Access to phases of coherent phonon excitations by femtosecond ultraviolet photoelectron diffraction

M. Greif,[1] L. Kasmi,[2] L. Castiglioni,[1] M. Lucchini,[2] L. Gallmann,[2,3] U. Keller,[2] J. Osterwalder,[1] and M. Hengsberger[1]

[1]*Department of Physics, University of Zürich, Winterthurerstrasse 190, 8057 Zürich, Switzerland*

[2]*Department of Physics, ETH Zürich, Auguste-Piccard-Hof 1, 8093 Zürich, Switzerland*

[3]*Institute of Applied Physics, University of Bern, 3012 Bern, Switzerland*

(Dated: August 22, 2016)

Abstract

Coherent phonons are an excellent tool to investigate the interplay between electronic and structural dynamics. The displacive excitation of coherent phonons in elemental bismuth is one of the most widely studied processes for this purpose. We employ time-resolved photoelectron diffraction to access the structural dynamics by recording the photoemission intensity from one initial state as function of emission angle. In comparison with tight-binding and single-scattering cluster calculations, this allows electronic and structural effects to be disentangled. Hence, the full dynamics of the hot electron gas and of coherently excited phonons can be accessed in a single experiment. As a major result the phase lag between the coherent phonons and the modulation of the electronic structure can be determined with high precision. The phonon phase lag with respect to the modulation of the electronic structure is about 2.85 ± 0.21 rad, thus significantly smaller than π. The difference is not due to phonon decay by energy dissipation into low-energy modes, but rather caused by the very early evolution of the highly excited electron distribution.

I. INTRODUCTION

The dynamics of coherently excited phonons are a topic of intense research. One reason for this is the strong signal modulation in optical reflectivity or x-ray diffraction, which allow one to study the subtle interplay between electronic and structural degrees of freedom of solids: In a simple model, phonons are kick-started coherently by a short pulse promoting electrons into unoccupied states and shifting the atomic equilibrium positions. This mechanism was termed displacive excitation of coherent phonons (DECP)[1] and was theoretically treated e.g. in Refs. 2 and 3. As a consequence of the electronic response to the lattice modulation, the phonon mode then drives an oscillation of the electronic charge density. In a classical picture, this corresponds to a harmonic oscillator (electrons) with the plasma frequency being its natural frequency, which is driven by the phonons at the frequency of the phonon mode. The phase lag between the forced oscillation and the driving force is determined by the ratio of friction represented by the electron population decay rate and the phonon frequency. In the present paper we will show that the full dynamics and the phases of the different degrees of freedom can be accessed in a single experiment by using the well-known coherent phonon excitation in Bi as a model system.

Bi crystallizes in the rhombohedral A7 structure which results from the simple cubic lattice by two distortions: A slight displacement of the two fcc sublattices along the body diagonal [111] and a stretch of the cube along [111][4]. Large portions of the Fermi surface of Bi collapse by nesting and the bulk electronic structure becomes semi-metallic with very small density of states (DOS) at the Fermi energy E_F. The result is a stack of layers of hexagonal symmetry along the trigonal axis [111]. The distance between two adjacent layers alternates due to the displacement of the sublattices. This yields a bilayer structure which is quantified by a parameter x, which defines the distance between the two basis atoms of the unit cell in units of the hexagonal lattice constant c along the trigonal axis. For a cubic lattice $x = 0.5$, whereas for the equilibrium rhombohedral Bi lattice $x = 0.467$. Upon absorption of infrared light, electrons are promoted into unoccupied states. This excitation corresponds to a shift of the charge density in real space from within a bilayer to the space between the bilayers[5]. The equilibrium positions of the atoms move outward toward the positions of the cubic structure. This situation corresponds to a stretched spring which is released. The atoms start to oscillate around the new transient equilibrium positions.

In case of a light pulse, which is shorter than half the period of the lattice vibration, all atoms oscillate coherently along the trigonal axis. The optical phonon is the A_{1g} mode, what could be corroborated in many optical studies and by time-resolved x-ray and electron diffraction[1,6–11].

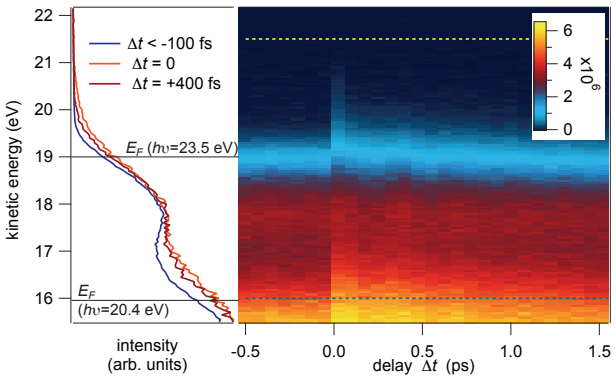

FIG. 1. (Color online) Photoemission spectra taken in normal emission. Two-dimensional (2D) data set representing the photoemission intensity at $\overline{\Gamma}$ versus kinetic energy (vertical axis) and pump-probe delay (horizontal axis). The intensity was integrated over 10° of the angular axis of the detector. Positive delays correspond to the XUV pulse arriving after the IR pump pulse. On the left-hand-side, energy distributions at different delays are shown with the two Fermi edges at about 16 and 19 eV indicated by horizontal lines. The dashed lines in the delay scan limit the integration range in energy over the valence band and excited states, i.e. about 5.5 eV around the Fermi edge at the higher photon energy.

Here we employ time- and angle-resolved photoelectron spectroscopy (tr-ARPES). The sensitivity of tr-ARPES to transient electronic structure changes following coherent phonon excitation allows one to investigate the influence of phonon excitations on electronic states in complex and strongly correlated systems like charge-density-wave systems[12,13], high-T_c superconductors[14], and topological insulators[15] and metals[16]. The angular intensity distribution of the photoelectrons is furthermore modulated by interference effects of scattered photoelectron waves and, thereby, provides direct information about the *atomic* structure of the surface. This effect is called photoelectron diffraction and can be seen in angular distributions excited by x-rays (XPD)[17,18] or ultraviolet light (UPD)[19–21]. We demonstrate

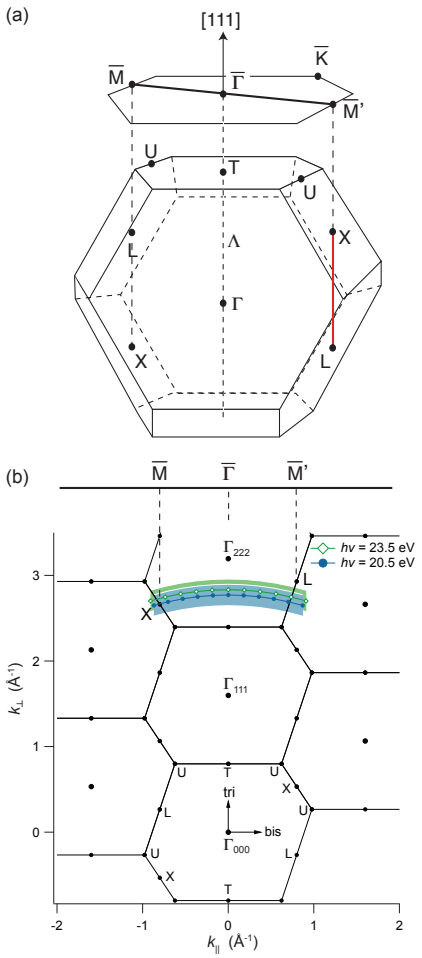

FIG. 2. (Color online) Reciprocal space representation. (a) Plot of the bulk and surface Brillouin zone (BZ) of the A7-lattice with high-symmetry points. The red line between X and L will be referred to in Fig. 5. (b) Cut through the BZ along the bulk mirror plane $\overline{\mathrm{M\Gamma M}}'$ in the periodic zone scheme. The positions of the direct transitions for $h\nu = 20.4$ eV and $h\nu = 23.5$ eV are shown by blue solid circles and green open diamonds, respectively, for steps in 5° in emission angle and electrons emitted from the Fermi level E_F. The photoemission final state was computed using free-electron like states with band bottom $E_0 - E_F = -12.8$ eV and effective mass $m^\star = 0.88\, m_e$, where m_e is the electron rest mass[29]. The broadening in the momentum perpendicular to the surface $k_\perp$ due to the short escape depth of about 8-9 Å[30] is indicated by color shading.

that the dynamics of the full process can be investigated by tr-ARPES and *photoelectron diffraction* using light from a high-harmonic laboratory source. While the electron dynamics after absorption of the pump pulse occur as transient occupation of states above E_F,

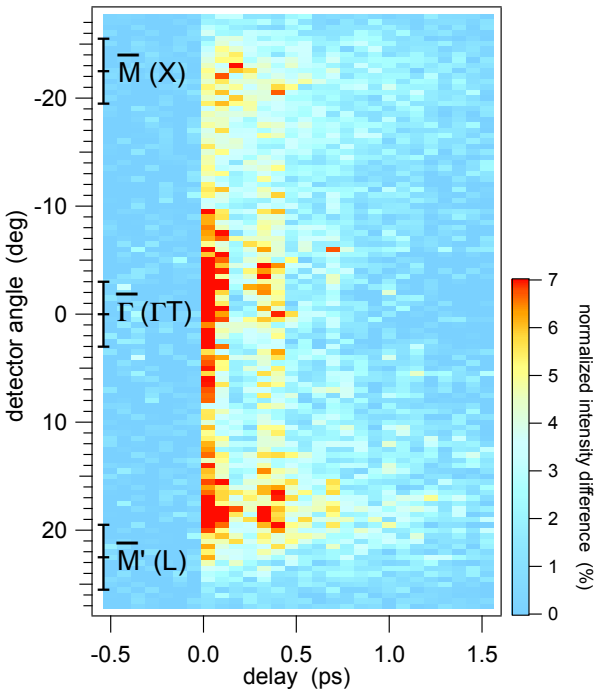

FIG. 3. (Color online) Photoemission data taken near normal emission as function of delay. Angular intensity distribution integrated over energy between the two dashed lines shown in Fig. 1. The curves at negative delays were averaged and subtracted. The center corresponds to normal emission $\overline{\Gamma}$, the outer extrema at emission angles of $\theta = \pm 22.5°$ to emission from the border of the surface Brillouin zone, $\overline{\mathrm{M}}$ and $\overline{\mathrm{M}}'$. The bars beside the symmetry labels indicate the integration ranges for the curves shown in Fig. 4.

the coherent phonon oscillations lead to intensity oscillations in the photoemission spectra. These modulations may be of both, electronic (DOS) and structural (diffraction) origin. By comparing the energy and the angular intensity distribution with tight-binding[22] and single-scattering cluster calculations (SSC,[23]) one is able to disentangle transient electronic and structural changes and to determine the phase lag between electronic excitation and the coherent phonon mode. The phase of the structural modulation is in excellent agreement with the phonon phase extracted from optical data[2,24]. This underlines the fact that tr-ARPES can provide direct information about the electronic and atomic structure within a single experiment.

II. EXPERIMENT

The Bi(111) surface was prepared by cycles of ion sputtering (1 keV Ar^+) and healing from sputter damage at 300 K. The quality of the surface was monitored by means of photoelectron spectroscopy and diffraction and low-energy electron diffraction. For time-resolved experiments, the photoelectrons were excited using extreme ultraviolet (XUV) light from the high-harmonic source attoline[25,26]. Using a combination of a 200 nm Sn filter and spectral cutoff, a spectrum consisting of two dominant harmonics was generated. The photon energies were 20.4 eV and 23.5 eV and the resulting photoemission spectra are superpositions of two spectra excited by these two lines. The incident fluence of the 800 nm infrared (IR) pump pulse was ≈ 1.6 J/cm^2 at normal incidence, and the overall temporal resolution was 25 fs. Both, XUV and IR pulses were p-polarized, and the angle between light incidence and the axis of the electron spectrometer was 45°. The photoemission yield from an argon gas-jet was recorded simultaneously and used to normalize the data for XUV fluctuations[26,27]. Photoelectrons were detected in a SPECS Phoibos 150 analyzer with wide-angle lens. The two-dimensional detector has an energy dispersive dimension parallel to the plane of light incidence and an angular axis which covers a range of ±30° with a resolution better than ±0.5°. Thus, points in reciprocal space can be accessed by rotating the sample and by choosing the proper detector window[28]. All data shown were taken with the sample held at room temperature.

III. TRANSIENT VALENCE BAND SPECTRA

In Fig. 1 we show the photoemission spectra taken in normal emission $\overline{\Gamma}$ as function of delay between 800 nm pump and XUV probe pulse in a false-color plot. Since the photon spectrum is dominated by two harmonics, the cutoff at E_F and the valence bands appear twice. At time delay zero a steep increase in intensity can be seen as a consequence of the excitation of electrons to unoccupied states above E_F. The increase is followed by an exponential decay. On top of the decay an intensity modulation is observed with a period of about 360 fs or a frequency of 2.76 THz. The value agrees with data published for an absorbed fluence of 0.9 mJ/cm^2[10]. It is important to note here that the modulation phase is such that the increasing edge is followed by a minimum and then by a maximum at about

360 fs.

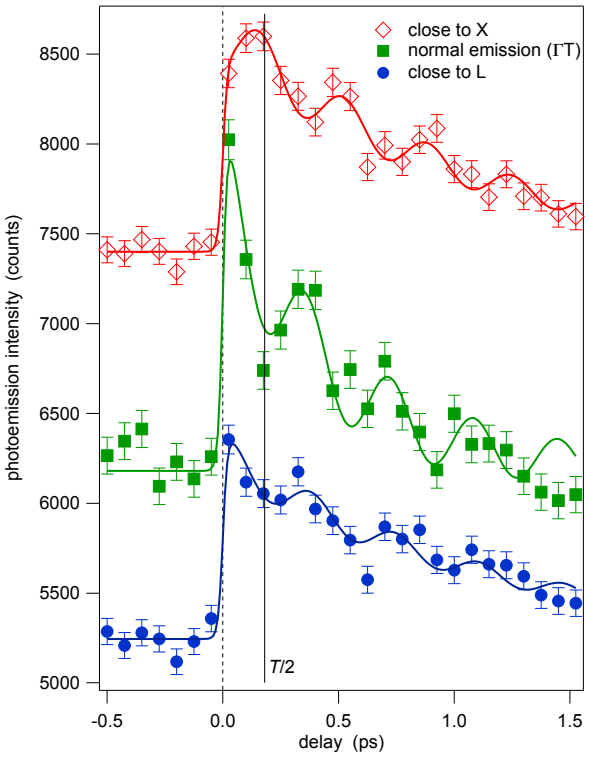

FIG. 4. (Color online) Cross-correlation traces extracted from the 2D data set from Fig. 3 for the high-symmetry points of the surface Brillouin zone. From top to bottom: The transients at $\overline{\mathrm{M}}$ (red open diamonds, bulk: X), $\overline{\Gamma}$(green solid squares, on ΓT-line), and $\overline{\mathrm{M}}'$(blue solid circles, L). The curves are offset vertically for the sake of clarity. The lines are fits of model curves and the error bars denote the statistical uncertainties. The delay zero and half a phonon period $T/2$ are indicated.

The generation of the hot-electron gas at delay zero can be modeled by decoupling electronic and lattice temperature; assuming thermal equilibrium within the electron gas only, the excess energy of the electron gas can be converted into an electronic temperature of about 2000 K[16?] . The modulations were already investigated previously with tr-ARPES and attributed to transient changes in the bulk electronic structure caused by the coherent excitation of A_{1g} phonons[?] . The angular dimension of the 2D-detector allows the transient photoemission spectra to be recorded in parallel over a range of $\pm 30°$ in emission angle[28]. In Fig. 2(a) the bulk and surface Brillouin zones (BZ) are shown. If the sample is oriented with its normal along the central axis of the analyzer, the reciprocal space covered

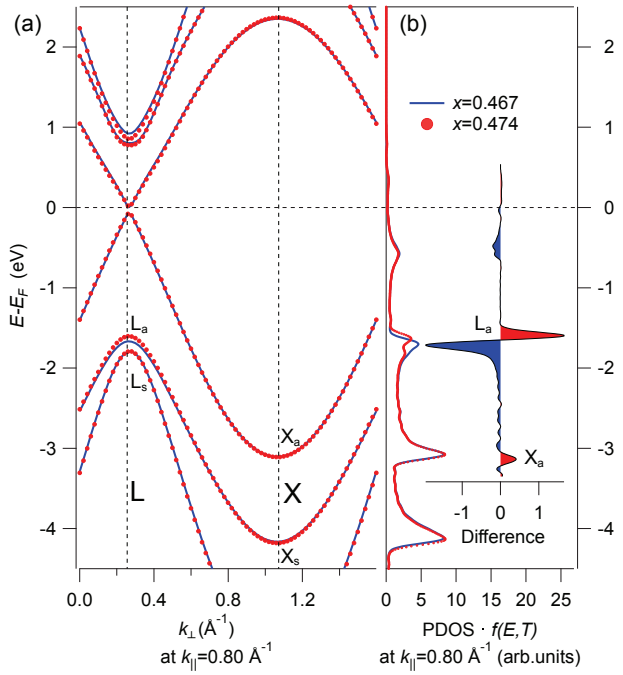

FIG. 5. (Color online) Band structure and photoemission density of states (PDOS) along the line XL of the bulk BZ or $\overline{\mathrm{M}}'(k_{\|} = 0.80$ Å$^{-1})$, indicated by a red line in Fig. 2(a). (a) Energy dispersion $E(k_{\perp})$ along XL calculated using the tight-binding scheme[22] for the equilibrium structure (blue lines, $x = 0.467$) and the maximum phonon amplitude (red circles, $x = 0.474$). The L and X points are marked. (b) PDOS obtained by integrating the inverse group velocity over a volume corresponding to the detection window of the experiment for the equilibrium lattice (blue curve) and the case of maximum distortion (red circles). The results were multiplied by the Fermi-Dirac distribution for a temperature of 2000 K. The difference in PDOS is shown for the energy integration range (same units than for PDOS). The symmetry labels are taken from Ref. 31. The integral underneath the color shaded curve yields the net modulation of the PDOS upon lattice distortion. Thus the large blue shaded part leads to an overall net decrease of the PDOS in the distorted state.

by the detector is a line from $\overline{\mathrm{M}}$ to $\overline{\mathrm{M}}'$ in the surface BZ within the mirror plane of bulk Bi. Both points are projections of the bulk high-symmetry points X *and* L, as can be seen in Fig. 2(a). In order to identify the bulk final state momenta of the transitions, the final state can be modeled with a free-electron-like parabolic dispersion. The parameters can be taken from photon-energy dependent photoemission experiments. Using the inner potential

and the effective mass of Jezequel an co-workers[29] we can deduce the final state momenta. The momenta are shown in Fig. 2(b) in the mirror plane. Despite the broadening in $k_\perp$ due to the finite escape photoelectron escape depth, the transitions are fairly well localized in reciprocal space. We find that photoelectrons detected at $\overline{\mathrm{M}}$ correspond to final and initial states at the bulk X point, those at $\overline{\mathrm{M}}'$ to states at the bulk L point. Photoelectrons detected at normal emission originate from states midway between the bulk Γ and T points. For convenience we will refer to all these transitions as transitions from X, L, and ΓT for the remainder of this manuscript.

The data recorded in parallel along X-ΓT-L are shown in Fig. 3 as difference plot in which the data at negative delays have been subtracted. Again, the oscillations are well observable over at least three phonon periods. Figure 4 shows the transients obtained by integration of the 2D data set from Fig. 3 around the main symmetry points ΓT, X, and L. All angle-resolved transients were fitted by the same generic function, which is a superposition of an exponentially decaying hot-electron distribution modulated by an oscillating cosine function with a phase offset:

$$\Delta I(t) = I_1 \cdot \Theta(t)\, e^{-t/\tau_e} \cdot \left(1 + I_2 \cos(\Omega t - \varphi) e^{-t/\tau_p}\right). \qquad (1)$$

$\Theta(t)$ denotes a sigmoid edge function, τ_e and τ_p the decay time constants of the electronic excitations and the phonon modulations, respectively, $\Omega = 2\pi\nu$ the $\mathrm{A_{1g}}$ frequency, and φ the phase with respect to the delay zero $t = 0$. I_1 and I_2 are intensity scales.

In the data taken at ΓT, a cosine-like oscillation of the valence band intensity is observed. The trace at L agrees qualitatively with the one at normal emission ΓTwith a slightly different phase and a longer decay time of $\tau_e(\mathrm{L}) = 1.1$ ps as compared to $\tau_e(\Gamma\mathrm{T}) = 0.44$ ps at ΓT. Interestingly, the modulation at X is markedly different: here the initial edge at delay zero is followed by a further increase reaching an intensity *maximum* after half the $\mathrm{A_{1g}}$ phonon period rather than an immediate intensity drop. The exponential decay time of $\tau_e(\mathrm{X}) = 1.1$ ps is close to the value at L.

We performed tight-binding calculations[22] once for the equilibrium lattice and once for the distorted lattice corresponding to the maximum $\mathrm{A_{1g}}$ amplitude of $\Delta x\, c = 3.5 \times 10^{-3} c \approx 0.04$ Å expected for the fluence used here[9,10]. The resulting band structure along the line XL is shown in Fig. 5(a). The so-called photoemission density of states (PDOS) is then obtained by integrating the density of states over a small volume in reciprocal space which

matches the solid angle covered by the detector and is centered at the initial state momenta where the photo-excitation takes place. The calculations for ΓT and L predict a net *decrease* of the PDOS upon increasing distortion away from the rhombohedral and towards the simple cubic lattice, as shown by the change of bands L_a and L_s and the corresponding net change in integrated PDOS in Fig. 5(b). Thus, the photoemission intensity modulation shows a minimum for maximum distortion at half a phonon period. The anisotropy of the modulation, i.e. the ratio of the modulation and the signal at negative time delays, for this fluence is evaluated by integrating the transient PDOS over the energy range given in Fig. 1; we obtain an anisotropy of about 5% at L and ΓT, and less than 1% at X.

Thus, the following picture emerges from the data and the tight-binding calculations: The unoccupied bulk DOS at the L-point is dominated by the electron pockets at E_F. Electrons excited by the pump pulse lose energy in scattering events and move down in the conduction band. Excited carriers accumulate at the bottom of the conduction band at the L-point. That is why the initial increase at delay zero is less pronounced at L than at ΓT, and the cross-correlation trace exhibits a longer time constant. In contrast to L, the X-point exhibits a large energy gap around E_F. The photoemission intensity at X is solely due to indirect phonon-assisted transitions[32] and photoelectron diffraction effects, as can be seen from the band structure and photoemission density of states (PDOS) displayed in Fig. 5, where all peaks in the spectra within the relevant energy range can be attributed to flat bands at L. The probability of indirect transitions depends on the lattice temperature, which increases on much longer timescales than the one of interest here[10]. The diffraction effects are due to interference between directly emitted and scattered photoelectron waves. The structural distortion by the A_{1g} mode leads to a change in distance between emitter and scatterer along the [111]-axis and, thereby, to a displacement of the interference fringes. Depending on the solid angle sampled in the experiment, this shift of the fringes results in an increase or decrease in photoemission intensity. SSC calculations show that an increase of photoemission intensity at angles corresponding to emission from the X-point is expected for increasing lattice distortion, as can be seen in Fig. 6(a). This explains the shift of roughly π between the intensity modulations at the X-point ($\overline{\mathrm{M}}$) and at the ΓT- or L-point ($\overline{\mathrm{M}}'$).

We anticipate that the transient angular distribution caused by changes of the atomic positions leads to an intensity decrease at ΓTand L as well. The relative contributions of direct photoemission and (indirect) photoelectron diffraction effects are temperature-

dependent and can be modeled using Debye-Waller-like weighting factors[33,34]. Taking into account the momentum vector involved in the direct transitions as shown in Fig. 2(b), a Debye temperature of 112 K[35], and the sample temperature we arrive at a Debye-Waller factor larger than 0.9. Thus, the contributions of direct transitions (PDOS) and structural effects (diffraction) to the overall intensity modulation add up[33], but the contribution of the electronic response clearly dominates the signal modulation.

IV. TIME-RESOLVED PHOTOELECTRON DIFFRACTION

For a further investigation of diffraction effects, delay scans were conducted at different emission directions. It was shown previously that the full valence band must be integrated in energy in order to avoid effects due to electronic dispersion[19,20]. The regions probed by the photoemission process are sketched in Fig. 6(a) together with results from SSC calculations and the surface Brillouin zone. The patterns are displayed in parallel projection, *i.e.* linear in the momentum component parallel to the surface. The calculations were carried out using the three p-like bands as emitters. This is justified due to the large energy separation between s- and p-like bands and the roughly equal contributions of p_x, p_y, and p_z to the occupied DOS[36,37]. Moreover, as in the experiment, the patterns were computed for four equally spaced binding energies within the occupied p-bandwidth and for the two photon energies, and finally summed up.

We mainly focus onto two regions in reciprocal space: a line through the center (normal emission) along $\overline{\mathrm{M\Gamma M}}'$, which was already discussed in detail before, and a circular arc along the azimuthal angle and centered at $\phi \approx 150°$ and at a polar emission angle $\theta = 50°$. The SSC calculations are shown for the rhombohedral structure in the lower half on a grey scale. The upper half represents the difference between the scattering pattern for the maximum lattice distortion in our experiment and the equilibrium structure. A blue arrow indicates the position for the diffraction measurements, which was optimized for large scattering anisotropy and large transient change. We note that for both, the X-point and the position for the diffraction measurement, an increase in photoemission intensity with increasing lattice distortion is expected.

In Fig. 6(b) the photoemission intensity for emission in the direction indicated by the blue arrow is shown as function of time delay for two measurement modes of the hemispher-

ical electron analyzer: (i) a fixed-energy mode where the energy distribution over a limited range is imaged onto the two-dimensional detector, and (ii) a sweep mode, where the detector window is scanned over the energy spectrum. For the present work it is important to note that both modes yield comparable statistics and identical results for the curve fitting. At time delay zero, a slow increase is observed reaching maximum intensity $\approx 10\%$ above the base line after half a phonon period. For a more quantitative insight and comparison, all curves were fitted using the function given in Eq. (1) in a least-square fit by means of the Levenberg-Marquardt algorithm. In these fits, the phonon frequency and decay parameters were kept constant between measurements taken with the same fluence. The phonon damping parameter τ_p was inferred from the diffraction measurements at the X-point and at $\theta = 50°$. The results are summarized in Table I.

TABLE I. Offset phases φ_i, phonon frequency Ω, and time constants τ_e, τ_p obtained by fitting the data by Eq. (1). Note that the measurement at $\theta = 50°$ was taken for higher pump fluence than in normal emission. The errors are standard deviations of the fitting parameters.

$\vec{k}$	$\Omega/2\pi$ [THz]	offset phase φ_i [rad]	relevant decay time [ps]
ΓT	2.76 ± 0.10	-0.05 $\pm$0.25	$\tau_e(\Gamma\mathrm{T}) = 0.44 \pm 0.02$
L		+0.43 $\pm$0.39	$\tau_e(\mathrm{L}) = 1.10 \pm 0.12$
X		$+2.85 \pm 0.21$	$\tau_e(\mathrm{X}) = 1.02 \pm 0.02$
			$\tau_p(\mathrm{X}) = 1.33 \pm 0.96$
$\theta = 50°$	2.57 ± 0.10	+2.76 $\pm$0.25	$\tau_p = 0.6 \pm 0.07$

The frequency of the modulation is lower and the phonon scattering time smaller for the data taken at $\theta = 50°$ than for the data taken at X due to the increased fluence and the small angle of incidence for this measurement. The phase of the cosine function is shifted by 2.76 rad, in good agreement with the phase of the modulation at X: $\varphi_\mathrm{X} = 2.85$ rad. In order to be consistent throughout the analysis we will continue with the data from the X-point and use the other data sets for comparison only.

The phase $\varphi_\mathrm{X} = 2.85$ rad appears to be significantly smaller than π with respect to the electronic excitation. From a theoretical treatment of DECP[2], we adopt the following expression taking into account the scattering rates and the natural $\mathrm{A_{1g}}$ frequency $\Omega_0 =$

$2\pi \cdot 2.94$ THz:

$$\tan(\varphi - \pi) = -\frac{\tau_e^{-1} - \tau_p^{-1}}{\sqrt{\Omega_0^2 - \tau_p^{-2}}} = -\frac{\tau_e^{-1} - \tau_p^{-1}}{\Omega}\,. \tag{2}$$

Applied to our values, we obtain $\varphi - \pi \approx -0.013 \pm 0.03$ rad, which is far from our value $\varphi_{\mathrm{X}} - \pi = -0.29 \pm 0.21$ rad. Zeiger et al., and more recently Hase et al. investigated the $\mathrm{A_{1g}}$ mode by means of time-resolved reflectivity measurements and Raman spectroscopy. Despite the fact that reflectivity probes the joint density of states at the photon energy and thus averages over the whole BZ, they obtained a phonon phase lag with respect to time delay zero of 2.91 rad[2] and 2.87 rad[24], which is in excellent agreement with the value found here, however without the possibility of measuring simultaneously the momentum-resolved electronic response.

In order to elucidate this issue, we estimate the decay time constant necessary to obtain the observed phase shift φ_{X} and phonon softening. The experimental values lead to $\tau_e \approx 0.6$ ps, thus close to the decay time $\tau_e(\overline{\Gamma}) = 0.44$ ps of the initial hot-electron distribution. This suggests that the early dynamics of the hot electrons determine the phase lag between electrons and phonons. Indeed, the nuclear acceleration due to the large initial displacement of electronic charge density is expected to be stronger than for the subsequent phonon cycles. At the same time, the initial hot electron distribution decays fast leading to an initial overshooting and overdamping of the $\mathrm{A_{1g}}$ mode, which yet is fluence dependent as corroborated by comparing our data from the X-point and at $\theta = 50°$. In a recent time-resolved THz-spectroscopy study, the authors pointed out that the hot-electron dynamics might determine the phonon dynamics due to the fact that the complete thermalization of the electron-plasma takes place on a time scale longer than a phonon period[38]. Over longer timescales, one expects an equilibration of both frequencies and the phase lag to approach π. Unfortunately, an analysis of such subtle effects cannot be done using our photoemission data due to the long phonon periods and fast decay rates, which inhibit a reliable calculation of the phonon frequency at long delay times.

V. CONCLUSION

In conclusion, we presented a way to obtain full information about the dynamics of the electron-phonon system in a single experiment in bismuth by taking advantage of the power of time- and angle-resolved photoelectron spectroscopy and diffraction. We conjecture

that this way of taking and interpreting time- and angle-resolved photoemission data will become an important tool in the investigation of electronic and structural excitations and the interactions thereof, in particular when using high-harmonic generation with a high repetition-rate laser system[39,40].

As an example demonstrated here, this allows phases between atomic and electronic modulations to be measured simultaneously. We find that the phase lag can only correctly be reproduced using a simple model[2], if the early dynamics of the excited carrier distribution are taken into account.

ACKNOWLEDGMENTS

We thank Dominik Leuenberger and Peter Krüger for valuable discussions. We acknowledge financial support from the Swiss National Science Foundation through the NCCR MUST.

---

[1] T. K. Cheng, S. D. Brorson, A. S. Kazeroonian, J. S. Moodera, G. Dresselhaus, M. S. Dresselhaus, and E. P. Ippen, Appl. Phys. Lett. **57**, 1004 (1990).

[2] H. J. Zeiger, J. Vidal, T. K. Cheng, E. P. Ippen, G. Dresselhaus, and M. S. Dresselhaus, Phys. Rev. B **45**, 768 (1992).

[3] Y. Giret, A. Gellé, and B. Arnaud, Phys. Rev. Lett. **106**, 155503 (2011).

[4] V.S. Édel'man, Adv. Phys. **25**, 555 (1976).

[5] E. Papalazarou, J. Faure, J. Mauchain, M. Marsi, A. Taleb-Ibrahimi, I. Reshetnyak, A. van Roekeghem, I. Timrov, N. Vast, B. Arnaud, and L. Perfetti, Phys. Rev. Lett. **108**, 256808 (2012).

[6] P. Beaud, S. L. Johnson, A. Streun, R. Abela, D. Abramsohn, D. Grolimund, F. Krasniqi, T. Schmidt, V. Schlott, and G. Ingold, Physical Review Letters **99**, 174801 (2007).

[7] D. Boschetto, E. G. Gamaly, A. V. Rode, B. Luther-Davies, D. Glijer, T. Garl, O. Albert, A. Rousse, and J. Etchepare, Phys. Rev. Lett. **100** 027404 (2008).

[8] S. L. Johnson, P. Beaud, E. Vorobeva, C. J. Milne, E. D. Murray, S. Fahy, and G. Ingold, Phys. Rev. Lett. **102**, 175503 (2009).

[9] G. Sciaini, M. Harb, S. G. Kruglik, T. Payer, C. T. Hebeisen, F.-J. M. z. Heringdorf, M. Yamaguchi, M. H.-v. Hoegen, R. Ernstorfer, and R. J. D. Miller, Nature **457**, 56 (2009).

[10] D. M. Fritz, D. A. Reis, B. Adams, R. A. Akre, J. Arthur, C. Blome, P. H. Bucksbaum, A. L. Cavalieri, S. Engemann, S. Fahy, R. W. Falcone, P. H. Fuoss, K. J. Gaffney, M. J. George, J. Hajdu, M. P. Hertlein, P. B. Hillyard, M. Horn-von Hoegen, M. Kammler, J. Kaspar, R. Kienberger, P. Krejcik, S. H. Lee, A. M. Lindenberg, B. McFarland, D. Meyer, T. Montagne, E. D. Murray, A. J. Nelson, M. Nicoul, R. Pahl, J. Rudati, H. Schlarb, D. P. Siddons, K. Sokolowski-Tinten, T. Tschentscher, D. von der Linde, and J. B. Hastings, Science **315**, 633 (2007).

[11] A. Bugayev, A. Esmail, M. Abdel-Fattah, and H. E. Elsayed-Ali, AIP Advances **1**, 012117 (2011).

[12] L. Perfetti, P. A. Loukakos, M. Lisowski, U. Bovensiepen, H. Berger, S. Biermann, P. S. Cornaglia, A. Georges, and M. Wolf, Phys. Rev. Lett. **97**, 067402 (2006).

[13] D. Leuenberger, J. A. Sobota, S.-L. Yang, A. F. Kemper, P. Giraldo-Gallo, R. G. Moore, I. R. Fisher, P. S. Kirchmann, T. P. Devereaux, and Z.-X. Shen, Phys. Rev. B **91**, 201106 (2015).

[14] L. Perfetti, P. A. Loukakos, M. Lisowski, U. Bovensiepen, H. Eisaki, and M. Wolf, Phys. Rev. Lett. **99**, 197001 (2007).

[15] J. A. Sobota, S. Yang, J. G. Analytis, Y. L. Chen, I. R. Fisher, P. S. Kirchmann, and Z. X. Shen, Phys. Rev. Lett. **108**, 117403 (2012).

[16] D. Leuenberger, H. Yanagisawa, S. Roth, J. H. Dil, J. W. Wells, P. Hofmann, J. Osterwalder, and M. Hengsberger, Physical Review Letters **110**, 136806 (2013).

[17] D. Naumović, A. Stuck, T. Greber, J. Osterwalder, and L. Schlapbach, Phys. Rev. B **47**, 7462 (1993).

[18] J. Osterwalder, *Structural Effects in XPS and AES: Diffraction*, edited by D. Briggs and J. T. Grant, Surface Analysis by Auger and X-Ray Photoelectron Spectroscopy (IM Publications and Surface Spectra Limited, 2003).

[19] J. Osterwalder, T. Greber, P. Aebi, R. Fasel, and L. Schlapbach, Phys. Rev. B **53**, 10209 (1996).

[20] P. Krüger, F. Da Pieve, and J. Osterwalder, Phys. Rev. B **83**, 115437 (2011).

[21] M. Greif, L. Castiglioni, A. P. Seitsonen, S. Roth, J. Osterwalder, and M. Hengsberger, Phys. Rev. B **87**, 085429 (2013).

[22] Y. Liu and R. E. Allen, Phys. Rev. B **52**, 1566 (1995).

[23] P. J. Orders and C. S. Fadley, Phys. Rev. B **27**, 781 (1983).

[24] M. Hase, K. Mizoguchi, H. Harima, S.-i. Nakashima, and K. Sakai, Phys. Rev. B **58**, 5448 (1998).

[25] R. Locher, M. Lucchini, J. Herrmann, M. Sabbar, M. Weger, A. Ludwig, L. Castiglioni, M. Greif, M. Hengsberger, L. Gallmann, and U. Keller, Rev. Sci. Instr. **85**, 013113 (2014).

[26] R. Locher, L. Castiglioni, M. Lucchini, M. Greif, L. Gallmann, J. Osterwalder, M. Hengsberger, and U. Keller, Optica **2**, 405 (2015).

[27] M. Lucchini, L. Castiglioni, L. Kasmi, P. Kliuiev, A. Ludwig, M. Greif, J. Osterwalder, M. Hengsberger, L. Gallmann, and U. Keller, Phys. Rev. Lett. **115**, 137401 (2015).

[28] M. Greif, L. Castiglioni, D. Becker-Koch, J. Osterwalder, and M. Hengsberger, Journal of Electron Spectroscopy and Related Phenomena **197**, 30 (2014).

[29] G. Jezequel, J. Thomas, and I. Pollini, Phys. Rev. B **56**, 6620 (1997).

[30] A. Zangwil, *Physics at Surfaces* (Cambridge University Press, Cambridge, 1988)

.

[31] S. Golin, Phys. Rev. **166**, 643 (1968).

[32] G. Jezequel, A. Barski, P. Steiner, F. Solal, P. Roubin, R. Pinchaux, and Y. Petroff, Phys. Rev. B **30**, 4833 (1984).

[33] Z. Hussain, S. Kono, R. E. Connelly, and C. S. Fadley, Phys. Rev. Lett. **44**, 895 (1980).

[34] R. C. White, C. S. Fadley, M. Sagurton, and Z. Hussain, Phys. Rev. B **34**, 5226 (1986).

[35] O. Madelung, U. Rössler, and M. Schulz, eds., "Bismuth (bi) debye temperature, heat capacity, density, melting point," in *Non-Tetrahedrally Bonded Elements and Binary Compounds I* (Springer Berlin Heidelberg, Berlin, Heidelberg, 1998) pp. 1–3.

[36] X. Gonze, J.-P. Michenaud, and J.-P. Vigneron, Physica Scripta **37**, 785 (1988).

[37] G. Jezequel, Y. Petroff, R. Pinchaux, and F. Yndurain, Phys. Rev. B **33**, 4352 (1986).

[38] I. Timrov, T. Kampfrath, J. Faure, N. Vast, C. R. Ast, C. Frischkorn, M. Wolf, P. Gava, and L. Perfetti, Phys. Rev. B **85**, 155139 (2012).

[39] C. M. Heyl, J. Güdde, A. L'huillier, and U. Höfer, J. Phys. B-At. Mol. Opt. **45**, 074020 (2012).

[40] F. Emaury, A. Diebold, C. J. Saraceno, and U. Keller, Optica **2**, 980 (2015).

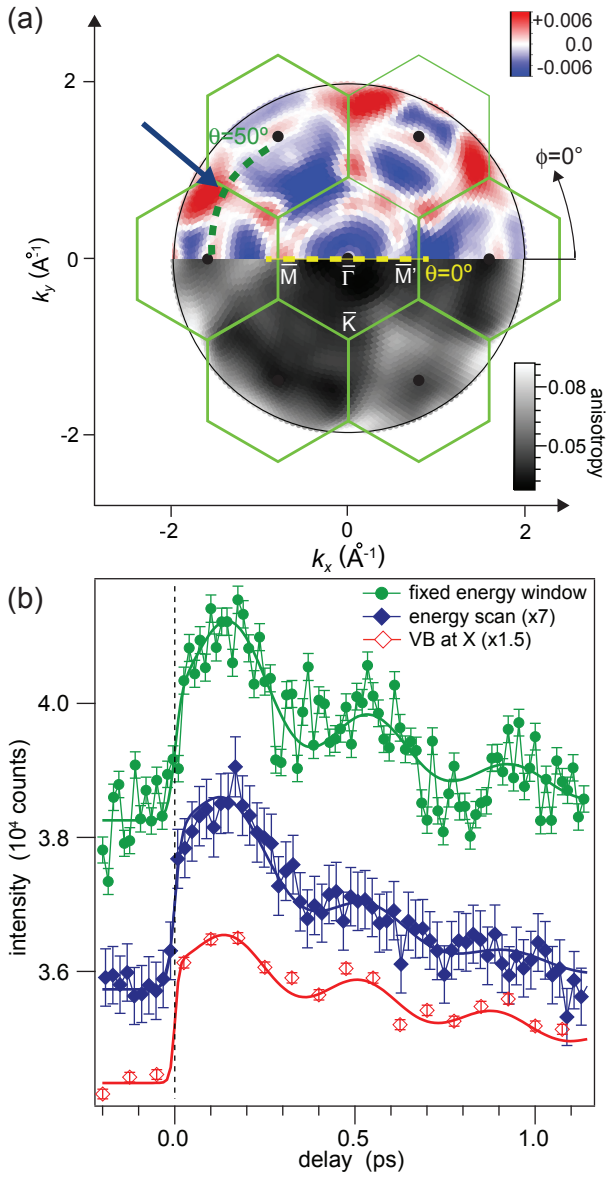

FIG. 6. (Color online) Time-resolved photoelectron diffraction data. (a) Scattering anisotropy from SSC calculations in parallel projection; the lower half represents the equilibrium state $x = 0.467$, the upper half the difference in scattering anisotropy between the distorted $x = 0.474$ and the equilibrium state (red color denotes higher intensity in the distorted state). The first surface Brillouin zone is shown as green lines with high-symmetry points. Note the three-fold symmetry of the Bi(111) surface. The yellow and green dashed curves correspond to measurements near normal emission (Fig. 3) and at $\theta = 50°$, respectively. (b) Scans taken with the detector centered at $\theta = 50°$ and $\phi = 150°$ indicated by the blue arrow in (a). The blue diamonds and solid green circles are experimental data integrated over a detector window of 10° for two different measurement modes of our hemispherical detector (see text for details). The red curve corresponds to the signal at X from Fig. 4. The solid lines are fits to the data.